Diffusion in grid turbulence of isotropic macro-particles using a Lagrangian stochastic method: Theory and validation

A. Joly,[1,a)] F. Moulin,[2] D. Violeau,[1] and D. Astruc[2]
[1]*Saint-Venant Laboratory for Hydraulics, Université Paris-Est, Joint Research Unit EDF/CETMEF/ENPC, Chatou 78401, France*
[2]*Université de Toulouse, INPT, UPS, IMFT, Allée Camille Soula, F-31400 Toulouse, France and CNRS, IMFT, F-31400 Toulouse, France*

The prediction of solid bodies transport (such as algae, debris, sediment grains, or corrosion deposits) is a necessary requirement in many industrial or environmental processes. The physical processes involved cover a wide range of processes, from tidal flow to turbulent eddies and particle drag. A stochastic model was therefore developed to link the different scales of the physical processes where it was assumed that the particles are dilute enough that they do not affect the flow or the motion of other particles while being large enough that each particle does not follow exactly the fluid motions (i.e., macro-particles). The stochastic model is built in such a way that it uses Reynolds-averaged fluid properties to predict trajectories of individual particles. This model was then tested using experimental measurements obtained for isotropic particles released in semi-homogeneous turbulence. The turbulent flow was generated using a pair of oscillating grids and was characterized using particle image velocimetry measurements. The trajectories of the particles were measured using a pair of high resolution cameras. The comparison between the experimental data and different numerical models gives satisfactory results.

I. INTRODUCTION

The presence of bodies in a flow and the transport patterns of these bodies is a classic problem in fluid mechanics. Whether it is the transport of sediments along a coastline, the apparition of air bubbles in pipe flow or aerosols released by fossil fuels it is important to develop tools predicting the motion of these particles, as they can hinder the operation of many industrial structures.

The model developed in this paper focuses on rigid particles. Furthermore, it is assumed that the particles within the fluid are dilute enough that they do not affect the flow or the motion of other particles. A non-dimensional number Ω_f, representing the volume fraction of particles, can be defined by

$$\Omega_f = \frac{N_r \Omega}{V_{ol}}, \tag{1}$$

where N_r is the total number of particles in the flow, Ω is the volume occupied by a single particle, and V_{ol} is the total volume occupied by the particles and the fluid. Following Elghobashi,[1] we can assume that the particle-laden flow can be modeled using one-way coupling (fluid-particle), if the volume fraction of particles Ω_f is lower than 10^{-6}. A one way fluid-particle coupling means that the information from the fluid is given to the particle motion, but there is no transfer of information from the particles to the fluid flow.

a)Electronic mail: antoine.joly@edf.fr.

This model was also developed for a class of particles that are large enough (or macro) that they do not follow exactly the motion of the fluid, yet they are small enough that the particles respond to some flow motions. Eaton and Fessler[2] have used the non-dimensional particle Stokes number St, given by the following equation:

$$\mathrm{St} = \frac{\tau_p}{\tau_s}, \tag{2a}$$

$$\tau_p = \frac{\left(2\rho_s + \rho_f\right) D^2}{36\mu}, \tag{2b}$$

$$\tau_s = \left(\frac{\nu}{\varepsilon}\right)^{\frac{1}{2}}, \tag{2c}$$

where ρ_s is the particle density, ρ_f is the fluid density, D is the particle characteristic length, μ is the dynamic viscosity, ν is the kinematic viscosity (defined by $\nu = \mu/\rho_f$), and ε is the dissipation rate of the turbulent kinetic energy.

The Stokes number of Eq. (2a) is a ratio of two characteristic times; τ_p which is the relaxation time for a particle experiencing only Stokes drag, and τ_s which is the characteristic time for the small turbulent eddies. Eaton and Fessler[2] show that particle with a Stokes number between 0.01 and 25 can be considered to be partially affected by the motion of the fluid. A more complete overview of particle-laden flow parameters can be found in Poelma, Westerweel, and Ooms.[3]

In addition, the particle-laden flow model presented in this paper will try to focus on environmental flows. Unlike most particle flows in industrial problems, for example, flows found in Uhlmann[4] or Minier and Peirano,[5] these flows require a large physical area modeled to predict the flow rate. For example, a model covering an area of a few kilometers squared solved for several hours is needed to predict the tidal evolution for a flow around a coastal industrial structure, see Salomonsen *et al.*[6] or Donaghay and Osborn.[7] However, the particles of interest in these environmental problems, such as algae, debris, or sediments, tend to respond to flow characteristics of a much smaller scale, such as turbulence induced diffusion or particle drag. It is too costly to run computer simulations that can model all the small scale effects in large environmental models, which is why a Lagrangian approach has been developed, for which a large scale numerical simulation can be run to predict the Reynolds-averaged flow properties, which are then used to consider small scale flow characteristics at the location of a particle. Furthermore, the particles present in such flows are very dilute, which tends to create large inhomogeneity in the solid mater field, which is better modeled using a Lagrangian method than an Eulerian method.

The model presented in this paper differentiates itself from other particle models specifically through the size of the particles and the nature of the coupling. In several models, the particles are considered very small, see Csanady,[8] Minier and Peirano,[5] or Sawford and Guest[9] for atmospheric or large gas-solid particle interactions models or Yeo *et al.*[10] for bubble or liquid-gas (with extensions to liquid-solid) interactions. Because of their relative size the physical properties can be greatly simplified, and therefore a focus is placed on modeling accurately the turbulence. However, in this case the particles are larger than the small scales of turbulence (but still small enough to be affected by the turbulent fluctuations), which will mean that the inertial properties of a body will have a dominant impact on the motion of the body, and therefore a relatively simple turbulence model will suffice.

The problem that inspired the development of the model presented in this paper is the short term transport (during one tide cycle) of algae in coastal waters, around industrial structures and harbours. To give an idea of their typical size, the particles can be considered to be smaller than one tenth of the large turbulent eddies in the flow and approximately ten times larger than small turbulent eddies. For more details on the type of particles considered refer to Joly.[11]

Although the model presented in this paper is specifically designed for environmental flows, it has properties which should be verified in a simplified flow regime, such as the diffusion of spheres in homogeneous isotropic turbulence. An experimental setup has been developed which allows semi-isotropic turbulence to be generated using a pair of oscillating grids. Particle image velocimetry then makes it possible to quantify the turbulent properties of the flow, and therefore the

flow conditions around released particles. The experimental results will be compared to numerical simulations using the model presented in this paper as well as other Lagrangian particle transport model.

The objective of the first part of this paper is, therefore, to present a Lagrangian model for the transport of solid bodies within a turbulent flow, whereas the second part aims to provide validations through the semi-isotropic turbulent flow of the experimental setup.

II. PARTICLE TRANSPORT MODEL

It was stated earlier that a particle trajectory will be influenced by the fluid motions. The turbulent structures in the flow will have diffusive effect on the particles, and therefore it is important to model the turbulent fluctuations of the flow around the body of interest. Because of the scale of the area of environmental flow problems,[7,12] compared to the size of relevant bodies, the approach chosen in this paper is that of a Lagrangian stochastic model to predict the fluid velocities at location of the body. This method allows to use a large scale model, such as Reynolds-averaged Navier-Stokes with k-ε closure, to predict the mean flow characteristics over the whole area of interest, which can then be imputed into a Lagrangian model to consider finer flow properties, such as turbulent velocity fluctuations, at the location of a particle.

The fluid in this paper will be considered incompressible, which is the case in most environmental hydraulic flows. As was stated in the Introduction, the model was developed for the case where the bodies are assumed to be sufficiently small that their presence does not affect the flow regime and diluted enough that the motion of one particle does not affect the flow or the motion of another particle in the absence of collisions. These hypotheses will therefore allow a one-way Lagrangian approach to be undertaken where the motion of the body depends on the fluid properties, but it does not affect the flow.

A. Stochastic turbulence model

Stochastic turbulence models rely on the idea that a turbulent flow velocity field can be separated into two parts, the mean flow velocities ($\overline{\mathbf{U}}$), and the fluctuations due to the turbulent eddies ($\mathbf{U}' = \mathbf{U} - \overline{\mathbf{U}}$). These turbulent fluctuations are then assumed to be a random process, which implies that an Eulerian probability density function (pdf) can be defined by the following equation:

$$f(\mathbf{u}; \mathbf{x}, t) = p\{\mathbf{U}(\mathbf{X}(t), t) = \mathbf{u}\}. \tag{3}$$

This function represents the probability p that at an instant in time, t, the fluid velocity $\mathbf{U}$ at location $\mathbf{X}(t)$ will be equal to the velocity $\mathbf{u}$. The transport equation of this pdf, as given by Pope,[13] is

$$\frac{\partial f}{\partial t} + u_i \frac{\partial f}{\partial x_i} = -\frac{\partial}{\partial u_i}\left[f \left\langle \frac{DU_i}{Dt} \middle| \mathbf{u} \right\rangle \right]. \tag{4}$$

In Eq. (4), and subsequently, the subscript i denotes a projection of the property along the Cartesian axis i. Furthermore, the symbol $|$ denotes a conditional probability (in this instance with respect to $\mathbf{u}$), and the symbol $\langle ... \rangle$ represents the probabilistic expectation. If the Navier-Stokes equations are used to solve $\frac{DU_i}{Dt}$, the transport equation (4) becomes

$$\frac{\partial f}{\partial t} + u_i \frac{\partial f}{\partial x_i} = \frac{1}{\rho_f} \frac{\partial \overline{P}}{\partial x_i} \frac{\partial f}{\partial u_i} - \frac{\partial}{\partial u_i}\left[f \left\langle \nu \nabla^2 U_i - \frac{1}{\rho_f} \frac{\partial P'}{\partial x_i} \middle| \mathbf{u} \right\rangle \right]. \tag{5}$$

In this equation, $\overline{P}$ and P' represent the mean pressure and its fluctuation due to turbulence, at location $\mathbf{X}(t)$. A model is then used to estimate the conditional expectation for the viscous effects ($\nu \nabla^2 U_i$) and the pressure fluctuations ($\frac{1}{\rho_f} \frac{\partial P'}{\partial x_i}$). The most commonly used model is the generalized Langevin model, which corresponds to the minimal modifications that need to be applied to the Langevin equation to be consistent with the mean momentum and kinetic energy equations. Using

this approach, Pope[13] has then written the following closed form for pdf transport equation (5):

$$\frac{\partial f}{\partial t} + u_i \frac{\partial f}{\partial x_i} - \frac{1}{\rho_f} \frac{\partial \overline{P}}{\partial x_i} \frac{\partial f}{\partial u_i} = -\frac{\partial}{\partial u_i}\left[f G_{ij}(u_j - \overline{U_j}) \right] + \frac{1}{2} C_0 \varepsilon \frac{\partial^2 f}{\partial u_i \partial u_i}. \tag{6}$$

The value ε is the dissipation rate of the turbulent kinetic energy, and the coefficients $G_{ij}(\mathbf{x}, t)$ and $C_0(\mathbf{x}, t)$ model together the viscous effects and the pressure fluctuations. These terms depend on the local values of $\overline{U_i' U_j'}$, ε, and $\partial \overline{U_i} / \partial x_j$. The simplest form of these terms (for which the model can be called simplified Langevin model) is applicable to a non-homogeneous isotropic turbulence and considers the smallest turbulent eddies as white noise. Pope[13] has then defined these values as

$$G_{ij} = -C_R \frac{\varepsilon}{k} \delta_{ij}, \tag{7}$$

$$C_0 = 2.1. \tag{8}$$

The quantity k is the turbulent kinetic energy ($k = \frac{1}{2}\overline{U_i' U_i'}$), and the coefficient C_R is equal to $\frac{1}{2} + \frac{3}{4} C_0$.

Equation (6) is written in its Eulerian form; however, we are looking for a Lagrangian model. The relationship between the Eulerian function (f) and its Lagrangian counterpart (f_L) is given by the following equation in incompressible fluids:[13]

$$f(\mathbf{u}; \mathbf{x}, t) = \int f_L(\mathbf{u}, \mathbf{x}; t | \mathbf{Y}) \, d\mathbf{Y}. \tag{9}$$

Using this relationship Pope[13] has rewritten Eq. (6) into

$$dU_i = -\frac{1}{\rho_f} \frac{\partial \overline{P}}{\partial x_i} dt - C_R \frac{\varepsilon}{k} \left(U_i - \overline{U_i} \right) dt + \sqrt{C_0 \varepsilon} \, dW_i, \tag{10}$$

where dW_i is a Wiener process for which it is known using Ito stochastic integrals[14] that

$$\langle dW_i \rangle = 0, \tag{11}$$

$$\langle dW_i dW_j \rangle = dt \delta_{ij}. \tag{12}$$

It should be specified once more that for numerical applications the mean fluid properties $\overline{P}$, $\overline{\mathbf{U}}$, k, and ε need to be solved using another model; such as a Reynolds averaged Navier-Stokes model with k-ε closure.

Pope[15] gives a detailed analysis of this model, and a description of more complete stochastic turbulence models can be found in Pope.[13] This turbulence model, however, was chosen for its simple implementation, as in hydraulic environmental flows it is usually difficult to obtain finer mean fluid properties required by more advanced turbulence models.

Furthermore, the explicit resolution of Eq. (10) is subjected to strong constraints on the numerical time step,[5] which needs to be large compared to the characteristic time of the small turbulent eddies ($\tau_s = \sqrt{\frac{\nu}{\varepsilon}}$), but remain smaller than the characteristic time of the large turbulent eddies ($\tau_l = \frac{k}{\varepsilon}$). Because of these constraints, the solid body transport equations are solved using a semi-analytical method, described in Sec. II D.

B. Dynamic properties of a solid isotropic body in a fluid

There are several forces which drive the motion of a solid body inside a fluid,[16,17] but the most important forces, considering the scales of the flow and the bodies of interest (defined through the values of Ω_f and St presented in the Introduction), will be the momentum of the fluid, the added mass of the body, the drag force, the basset history force, and the gravity force. The volume fraction of the particle (Ω_f) is assumed smaller than 10^{-6}. Therefore, a one-way fluid-particle coupling is sufficient to model the particle transport,[1] or in other words the particles do not affect the fluid motion or each other. As it is assumed that particles do not affect the flow, the size of each particle will entail that when it experiences acceleration from the flow, the flow variations are negligible along a length scale of the same order as its characteristic size. This assumption implies that the model

will ignore the local fluid vorticity and velocity gradients of the turbulent structures, and therefore the modeled particles will not rotate, and keep the same orientation through time. This then leads to the assumption that the lift forces, which are dependent on the surrounding velocity gradients and rotational rates of the fluid or particle, are negligible. More information on the effect of shear flows and freely rotating spheres can be found in Bagchi and Balachandar.[18] Furthermore, the finite size of the particles will result in a filtering of the turbulence. Yeo *et al.*[10] have given evidence to the fact that turbulent eddies of size smaller than that of the particle will not affect the motion of the body.

Hence, the momentum of a solid body of volume Ω and mass m transported at a velocity $\mathbf{V}$ (where V_i represents the ith component of the particle velocity) inside a flow of velocity $\mathbf{U}$ and constant density ρ_f, is given in the following equation:

$$\begin{aligned} m\frac{dV_i}{dt} &= \rho_f \Omega \frac{dU_i}{dt} - M_{ij}\frac{d}{dt}(V_i - U_i) \\ &\quad + \frac{1}{2}\rho_f S C_D(\mathrm{Re})\,|\mathbf{U}-\mathbf{V}|\,(U_i - V_i) \\ &\quad + (m - \rho_f \Omega) g_i \\ &\quad + 6D^2 \rho_f \sqrt{\pi \nu} \int_{-\infty}^{t} \frac{1}{\sqrt{t-s}} \frac{d}{dt}(U_i - V_i)\, ds, \end{aligned} \tag{13}$$

where M_{ij} is the added mass tensor of the body, S is its cross-sectional area, D is its characteristic size, g_i is the vectorial notation of the acceleration due to gravity, and C_D is the drag coefficient, which is a function of the particle Reynolds number Re,

$$\mathrm{Re} = \frac{|\mathbf{U}-\mathbf{V}|\,D}{\nu} \tag{14}$$

with ν being the fluid molecular kinematic viscosity, and the mass of the body is given by $m = \rho_s \Omega$, with ρ_s being its density.

The Basset history force F_{Basset}, given by the last line of Eq. (13) is written in its small particle formulation. This formulation was chosen, as a more complete formulation would require more information about the flow surrounding the particle than would be typically available in environmental flow. Even in this current formulation, it is difficult to solve and is often neglected. The method used in this paper to solve for this force is the method developed by van Hinsberg, ten Thije Boonkkamp, and Clercx.[19] In this method part of the integral is assumed to be linear, and it is solved for inside a numerical window. Outside this window, the tail of the Basset force is assumed to be exponentially decreasing. It is given by the following equation:

$$\begin{aligned} F_{Basset} &= \frac{4}{3} C_B \psi_0 \sqrt{\Delta t} + \frac{2}{3} C_B \psi_N \sqrt{\Delta t}\left(3\sqrt{N} + 2(N-1)^{\frac{3}{2}} - 2N^{\frac{3}{2}}\right) \\ &\quad + \frac{4}{3} C_B \sqrt{\Delta t} \sum_{n=1}^{N-1} \psi_n \left[(n-1)^{\frac{3}{2}} - 2n^{\frac{3}{2}} + (n+1)^{\frac{3}{2}}\right] \\ &\quad + \sum_{p=1}^{q} a_p F_p(t) + a_p \exp\left(\frac{-\Delta t}{2\widetilde{t_p} t_{win}}\right) F_p(t - \Delta t), \end{aligned} \tag{15}$$

$$\begin{aligned} F_p(t) &= 2C_B \sqrt{e\widetilde{t_p} t_{win}} \exp\left(\frac{-1}{2\widetilde{t_p}}\right) \left\{ \psi_N \left[1 - \phi\left(\frac{-\Delta t}{2\widetilde{t_p} t_{win}}\right)\right] \right. \\ &\quad \left. + \psi_{N+1} \exp\left(\frac{\Delta t}{2\widetilde{t_p} t_{win}}\right) \left[\phi\left(\frac{\Delta t}{2\widetilde{t_p} t_{win}}\right) - 1\right] \right\}, \end{aligned} \tag{16}$$

$$\phi(z) = \frac{e^z - 1}{z}, \tag{17}$$

where $C_B = 6D^2\rho_f\sqrt{\pi\nu}$, $\psi = d/dt\,(U_i - V_i)$, for which the notation ψ_x stands for $\psi(t - x\Delta t)$, t_{win} is the time for which the integral in the Basset force is solved and which is subdivided into N sections, which defines $\Delta t = t_{win}/N$. It is recommended to ensure that $\Delta t = dt$. The integer q, a_p, and $\widetilde{t_p}$ are defined in van Hinsberg, ten Thije Boonkkamp, and Clercx.[19] Here, we choose t_{win} so that N is equal to 100. Larger values of N were also tested but did not improve accuracy.

Numerically, all of the components from this Basset formulation, which do not depend on the current time step will be assumed to be constant. Therefore, this formulation of the Basset force can be rewritten as

$$F_{Basset} = \frac{4}{3}C_B\sqrt{\Delta t}\left(\frac{dU_i}{dt} - \frac{dV_i}{dt}\right) + C_{Bas}, \tag{18}$$

$$\begin{aligned} C_{Bas} = {} & \frac{2}{3}C_B\psi_N\sqrt{\Delta t}\left(3\sqrt{N} + 2\,(N-1)^{\frac{3}{2}} - 2N^{\frac{3}{2}}\right) \\ & + \frac{4}{3}C_B\sqrt{\Delta t}\sum_{n=1}^{N-1}\psi_n\left[(n-1)^{\frac{3}{2}} - 2n^{\frac{3}{2}} + (n+1)^{\frac{3}{2}}\right] \\ & + F_{tail}, \end{aligned} \tag{19}$$

$$F_{tail} = \sum_{p=1}^{q} a_p F_p(t) + a_p \exp\left(\frac{-\Delta t}{2\widetilde{t_p}t_{win}}\right) F_p(t - \Delta t). \tag{20}$$

Furthermore, the bodies are assumed to be isotropic (e.g., a sphere of diameter D), which simplifies the added mass tensor to $M_{ij} = M\delta_{ij}$. In the case of a sphere, considered later, the drag coefficient has been well documented in the literature (Almedeij[20] provides a review of different experimental results) and the added mass is given by $M = \frac{1}{2}\rho_f\Omega$.

In the case where the bodies of interest are not isotropic (for certain kinds of algae, for example), it should be noted that the isotropic body simplification can model similar statistics (for example, by averaging all the orientations possible and the folding of these bodies), however the drag coefficient or the added mass might need to be modified.

C. Two phase modeling

As Csanady[8] pointed out the motion of a solid particle, presented in Eq. (13), cannot be associated with the motion of a single fluid particle, modeled, for example, through Eq. (10), as these two particles will not travel at the same velocity. This effect is known as crossing trajectories. Therefore, the coupling of the fluid and the solid body velocities should be done through the fluid velocities as seen by the body U_i^*. A formulation for this velocity is given in Minier and Peirano,[5] where it is assumed that the external forces (gravity for example) play the major role in the decorrelation between the fluid velocity seen by the body and that of a fluid particle and it is assumed that the inertial properties of the particles play a minimal effect. This focus was done as it creates a mean drift between the fluid and particle velocities, and not an instantaneous one.[5] Equation (21) gives the general formulation for taking into account crossing trajectories effects and can be used in place of Eq. (10),

$$\begin{aligned} dU_i^*(t) = {} & -\frac{1}{\rho_f}\frac{\partial\overline{P}}{\partial x_i}dt + \left(\overline{V_i} - \overline{U_i}\right)\frac{\partial\overline{U_i}}{\partial x_j}dt - C_R\frac{\varepsilon}{\widetilde{k}}b_i\left(U_i^* - \overline{U_i}\right)dt \\ & + \sqrt{\varepsilon\left[C_0 b_i\frac{\widetilde{k}}{k} + \frac{2}{3}\left(b_i\frac{\widetilde{k}}{k} - 1\right)\right]}dW_i. \end{aligned} \tag{21}$$

In a similar fashion that $\overline{U_i}$ is the turbulence averaged fluid velocity, $\overline{V_i}$ is the turbulence averaged solid particle velocity. In addition, this equation is written for the assumption that the first coordinate

axis is aligned with the mean drift, therefore when modeling a change of variable might be required. The coefficient b_i represents the ratio between the Lagrangian integral timescale T_L and the integral timescale seen by the particle $T^*_{L,i}$. The timescales are given by the following equations:

$$T_L = \frac{1}{C_R}\frac{k}{\varepsilon}, \tag{22}$$

$$T^*_{L,i} = \frac{T_L}{b_i}. \tag{23}$$

And b_i is given by

$$b_1 = \sqrt{1 + 3T^2_{L/E}\frac{\left|\overline{\mathbf{V}} - \overline{\mathbf{U}}\right|^2}{2k}}, \tag{24a}$$

$$b_2 = b_3 = \sqrt{1 + 6T^2_{L/E}\frac{\left|\overline{\mathbf{V}} - \overline{\mathbf{U}}\right|^2}{k}} \tag{24b}$$

with the subscript 1 representing the direction longitudinal to the particle drift, and subscripts 2 and 3 directions transverse. These equations are dependent on the ratio between the Lagrangian integral timescale, and the Eulerian integral time scale. These are assumed to be approximately equal, $T_{L/E} = 1$, which implies that the decorrelation between the particle velocity and the fluid velocity is mainly due to external forcing on the particles, i.e., the "crossing trajectory effect." Furthermore, in Eq. (21) there is the introduction of a new kinetic energy given by

$$\widetilde{k} = \frac{3}{2}\frac{\sum_{i=1}^{3} b_i \overline{U_i'^2}}{\sum_{i=1}^{3} b_i} \tag{25}$$

with the symbol U_i' representing the fluid velocity fluctuations, $U_i' = U_i - \overline{U_i}$. This therefore gives a three step model for the transport of solid isotropic particles in turbulence:

$$dU_i^*(t) = -\frac{1}{T_t^*}U_i^* dt + C_i^* dt + B_i^* dW_i(t), \tag{26a}$$

$$dV_i(t) = F_a dU_i^* + F_b(U_i^* - V_i)dt + F_c dt, \tag{26b}$$

$$dX_i(t) = V_i dt, \tag{26c}$$

where the variable $\mathbf{X}(t)$ introduced here denotes the position of one solid particle of interest. In the system of Eq. (26), Eq. (10) has been rewritten into Eqs. (26a), and Eq. (13) has been rewritten into Eq. (26b), in order to make certain properties of these equations more visible. The new coefficients are given in Eqs. (27),

$$T_i^* = \frac{1}{C_R b_i}\frac{\widetilde{k}}{\varepsilon}, \tag{27a}$$

$$\tau_{part} = \frac{2\left(m + M + \frac{4}{3}C_B\sqrt{\Delta t}\right)}{\rho_f S C_D\,(\mathrm{Re})\left|\mathbf{U}^* - \mathbf{V}\right|}, \tag{27b}$$

$$C_i^* = -\frac{1}{\rho_f}\frac{\partial \overline{P}}{\partial x_i} + \left(\overline{V_i} - \overline{U_i}\right)\frac{\partial \overline{U_i}}{\partial x_j} + \frac{1}{T_i^*}\overline{U_i}, \tag{27c}$$

$$B_i^* = \sqrt{\varepsilon\left[C_0 b_i \frac{\widetilde{k}}{k} + \frac{2}{3}\left(b_i\frac{\widetilde{k}}{k} - 1\right)\right]}, \tag{27d}$$

$$F_a = \frac{\rho_f \Omega + M + \frac{4}{3} C_B \sqrt{\Delta t}}{m + M + \frac{4}{3} C_B \sqrt{\Delta t}}, \tag{27e}$$

$$F_b = \frac{1}{\tau_{part}}, \tag{27f}$$

$$F_c = \frac{\left(m - \rho_f \Omega\right) g_i + C_{Bas}}{m + M + \frac{4}{3} C_B \sqrt{\Delta t}}. \tag{27g}$$

This model still uses mean flow characteristics from a larger Eulerian model, in the same fashion as Eq. (10). T_i^* is a relative characteristic time for turbulence. C_i^* represents the ith component of the mean flow terms. The coefficient B_i^* models the variance of the stochastic term. In addition, F_b can be linked through Eq. (27f) to the particle relaxation time τ_{part}, which is a measure of the time necessary for a particle to adapt to changes in fluid velocity. F_a is linked to the mass characteristics of the body and F_c is linked to the buoyancy and gravity effects.

It should also be noted that for small particle Reynolds number, the drag force can be reduced to Stokes' drag, for which $C_D = 24/\mathrm{Re}$. Using this formulation of the drag force and neglecting the momentum and the Basset history force components ($M = 0$ and $C_B = 0$), then the particle relaxation time τ_{part} will be equal to the characteristic time τ_p of Eq. (2b).

Furthermore, considering the crossing trajectories increases the accuracy of the model, but it requires a level of information of the flow (through Eq. (25)) which is not usually available when modeling the environmental flow along a coastline (for example, if using the shallow water equation with a k-ε closure). Therefore, when we choose to neglect the crossing trajectories effect it should assumed that the fluid velocity seen by the particle is equal to the fluid velocity of a fluid particle ($\mathbf{U}^* = \mathbf{U}$). In this case, the constants become

$$T_i^* = T_L = \frac{1}{C_R} \frac{k}{\varepsilon}, \tag{28a}$$

$$C_i^* = C_i = -\frac{1}{\rho_f} \frac{\partial \overline{P}}{\partial x_i} - \frac{1}{T_L} \overline{U_i}, \tag{28b}$$

$$B_i^* = B = \sqrt{C_0 \varepsilon}. \tag{28c}$$

Numerically, this would imply that there is no mean relative velocity difference between particle and fluid velocities, which would indicate that the external forces have a negligible effect on the motion of a particle (during on time step), and therefore the diffusion of the solid particles might be overestimated.

D. The exact integrator method

Furthermore, it should be restated that this system of equation is subject to strong constraints on the numerical time step dt, as was mentioned earlier and in Minier and Peirano.[5] This is further emphasized through the two characteristic time T_i^* and τ_{part}, which require dt to be of the same order of magnitude to solve for the fluid and body velocities, respectively. Peirano *et al.*[21] presented a method for non-inertial solid particles which can circumvent these difficulties, and the same idea will be followed through here.

This method uses the idea that all the coefficients in the set of Eqs. (26) can be considered constant over the time interval $dt = t - t_0$. Therefore, if T_i^*, C_i^*, B_i^*, F_a, F_b, and F_c are constant an analytical equation can be obtained for the fluid velocity of the form[21] $U_i^*(t) = H_i(t) \exp\left(-\frac{t}{T_i^*}\right)$, where $H_i(t)$ is a function of time, and the derivative of the fluid velocity with respect to time is given by the following equation:

$$dU_i^*(t) = -\frac{1}{T_i^*} U_i^* dt + dH_i(t) \exp\left(-\frac{t}{T_i^*}\right). \tag{29}$$

Thus for the present problem $H_i(t)$ is a stochastic process defined by

$$dH_i(t) = \exp\left(\frac{t}{T_i^*}\right)\left[C_i^* dt + B_i^* dW_i(t)\right]. \tag{30}$$

The solution for H_i over the interval dt is

$$H_i(t) - H_i(t_0) = C_i^* T_i^* \left[\exp\left(\frac{t}{T_i^*}\right) - \exp\left(\frac{t_0}{T_i^*}\right)\right] + \int_{t_0}^{t} B_i^* \exp\left(\frac{s}{T_i^*}\right) dW_i(s). \tag{31}$$

This then gives the following equation for the fluid velocity at the location of the particle:

$$U_i^*(t) = \alpha_i^* U_i^*(t_0) + (1-\alpha_i^*) C_i^* T_i^* + \gamma_i(t) \tag{32}$$

with

$$\alpha_i^* = \exp\left(-\frac{dt}{T_i^*}\right), \tag{33}$$

where γ_i is a stochastic integral equal to

$$\gamma_i(t) = B_i^* \exp\left(-\frac{t}{T_i^*}\right) \int_{t_0}^{t} \exp\left(\frac{s}{T_i^*}\right) dW_i(s). \tag{34}$$

The same method can be applied to find the particle velocity

$$V_i(t) = \beta V_i(t_0) + (1-\beta)\left(C_i^* T_i^* + \frac{F_c}{F_b}\right) + \left(\alpha_i^* - \beta\right) \check{C}_i \left[U_i^*(t_0) - C_i^* T_i^*\right] + \Gamma_i(t) \tag{35}$$

with

$$\beta = \exp\left(-F_b dt\right), \tag{36}$$

$$\check{C}_i = \frac{T_i^* F_b - F_a}{T_i^* F_b - 1}, \tag{37}$$

where Γ_i is a stochastic integral equal to

$$\Gamma_i(t) = \check{C}_i \gamma_i(t) + B_i^* \left(F_a - \check{C}_i\right) \exp\left(-t F_b\right) \int_{t_0}^{t} \exp\left(F_b s\right) dW_i(s). \tag{38}$$

Finally to obtain the position of the solid particle at time t, a simple integration of the fluid velocity over the interval dt is performed

$$\begin{aligned} X_i(t) = X_i(t_0) + \frac{1-\beta}{F_b} V_i(t_0) + \left[dt - \frac{1-\beta}{F_b}\right]\left(C_i^* T_i^* + \frac{F_c}{F_b}\right) \\ + \check{C}_i [U_i^*(t_0) - C_i^* T_i^*] \left[\left(1-\alpha_i^*\right) T_i^* - \frac{1-\beta}{F_b}\right] + \Phi_i(t). \end{aligned} \tag{39}$$

In this final equation, the stochastic integral Φ_i is given by the following equation:

$$\begin{aligned} \Phi_i(t) = -\check{C}_i T_i^* \gamma_i(t) - \frac{1}{F_b}\left[\Gamma_i(t) - \check{C}_i \gamma_i(t)\right] \\ + \frac{B_i^*}{F_b}\left(T_i^* \check{C}_i F_b + F_a - \check{C}_i\right) \int_{t_0}^{t} dW_i(s). \end{aligned} \tag{40}$$

The three stochastic integrals, γ_i, Γ_i, and Φ_i, developed here are dependent. However, since they are stochastic integrals of deterministic functions, they can each be modeled by a centered Gaussian random variable[21] (i.e., with zero mean). Furthermore, it can be shown that a centered Gaussian vector can be expressed as the product of two matrices, the covariance matrix and a vector of independent standard random variables (zero mean and unitary standard deviation). Using the

Cholesky decomposition and an appropriate random number generator, these stochastic integrals can be modeled using the following equations:

$$\gamma_i = L_{11}\xi_{\gamma_i}, \tag{41a}$$

$$\Gamma_i = L_{21}\xi_{\gamma_i} + L_{22}\xi_{\Gamma_i}, \tag{41b}$$

$$\Phi_i = L_{31}\xi_{\gamma_i} + L_{32}\xi_{\Gamma_i} + L_{33}\xi_{\Phi_i}, \tag{41c}$$

where the ξ's are standard random variables and the coefficients L_{jk} are defined by

$$L_{11} = \sqrt{\langle \gamma_i^2 \rangle}, \tag{42a}$$

$$L_{21} = \frac{\langle \Gamma_i \gamma_i \rangle}{L_{11}}, \tag{42b}$$

$$L_{22} = \sqrt{\langle \Gamma_i^2 \rangle - L_{21}^2}, \tag{42c}$$

$$L_{31} = \frac{\langle \gamma_i \Phi_i \rangle}{L_{11}}, \tag{42d}$$

$$L_{32} = \frac{\langle \Gamma_i \Phi_i \rangle - L_{21}L_{31}}{L_{22}}, \tag{42e}$$

$$L_{33} = \sqrt{\langle \Phi_i^2 \rangle - L_{31}^2 - L_{32}^2}. \tag{42f}$$

The covariances, $\langle \gamma_i^2 \rangle$, $\langle \Gamma_i \gamma_i \rangle$, etc., are solved using the properties for stochastic integrals in Ito calculus

$$\langle \gamma_i^2 \rangle = \left(1 - \alpha_i^{*2}\right) B_i^{*2} \frac{T_i^*}{2}, \tag{43a}$$

$$\langle \Gamma_i^2 \rangle = \left(B_i^* \check{C}_i\right)^2 \left[\left(1 - \alpha_i^{*2}\right) \frac{T_i^*}{2} + \left(1 - \beta^2\right) \frac{\check{K}_i^2}{2F_b} + \left(1 - \alpha_i^* \beta\right) 2\check{Q}_i \right], \tag{43b}$$

$$\begin{aligned} \langle \Phi_i^2 \rangle = \left(B_i^* \check{C}_i\right)^2 \Bigg\{ & \check{G}_i^2 dt + \left(1 - \alpha_i^{*2}\right) \frac{T_i^{*3}}{2} + \left(1 - \beta^2\right) \frac{\check{K}_i^2}{2F_b^3} \\ & -2\check{G}_i \left[\left(1 - \alpha_i^*\right) T_i^{*2} + (1 - \beta) \frac{\check{K}_i}{F_b^2} \right] + 2\left(1 - \alpha_i^* \beta\right) \frac{\check{Q}_i T_i^*}{F_b} \Bigg\}, \end{aligned} \tag{43c}$$

$$\langle \gamma_i \Gamma_i \rangle = B_i^{*2} \check{C}_i \left[\left(1 - \alpha_i^{*2}\right) \frac{T_i^*}{2} + \left(1 - \alpha_i^* \beta\right) \check{Q}_i \right], \tag{43d}$$

$$\langle \gamma_i \Phi_i \rangle = B_i^{*2} \check{C}_i \left[\left(1 - \alpha_i^*\right) \check{G}_i T_i^* - \left(1 - \alpha_i^{*2}\right) \frac{T_i^{*2}}{2} - \left(1 - \alpha_i^* \beta\right) \frac{\check{Q}_i}{F_b} \right], \tag{43e}$$

$$\begin{aligned} \langle \Gamma_i \Phi_i \rangle = \left(B_i^* \check{C}_i\right)^2 \Bigg\{ & \left[\left(1 - \alpha_i^*\right) T_i^* + (1 - \beta) \frac{\check{K}_i}{F_b} \right] \check{G}_i - \left(1 - \alpha_i^{*2}\right) \frac{T_i^{*2}}{2} \\ & - \left(1 - \beta^2\right) \frac{\check{K}_i^2}{2F_b^2} - \left(1 - \alpha_i^* \beta\right) \frac{\check{K}_i T_i^*}{F_b} \Bigg\}. \end{aligned} \tag{43f}$$

With the following coefficients:

$$\check{K}_i = \frac{F_a}{\check{C}_i} - 1, \tag{44a}$$

$$\check{G}_i = T_i^* + \frac{\check{K}_i}{F_b}, \tag{44b}$$

$$\check{Q}_i = \frac{\check{K}_i T_i^*}{T_i^* F_b + 1}. \tag{44c}$$

It should be noted that this model reduces to the model presented by Peirano *et al.*[21] if the inertial terms and the Basset history force are ignored (i.e., $C_B = 0$, $C_{bas} = 0$, $F_a = 0$, and $M = 0$).

Furthermore, this method for solving the solid particle transport (Eqs. (26)) has defined solutions for the cases where the numerical time step is large or small compared to a characteristic time (T_L or τ_{part}), which was not the case for the explicit system of Eqs. (26). For example, when considering the transport of a fluid particle, if the time step dt is much larger than the turbulence characteristic time T_L, then the fluid velocity tends to $C_i T_L + \sqrt{\frac{B^2 T_L}{2}}\xi_{\gamma_i}$, which is the equation for Brownian motion. This is in agreement with the fact that all the turbulent eddies would appear as random independent events in this asymptotic limit.

III. EXPERIMENTAL TESTS

The model presented here is subject to strong hypotheses, especially on the solid body dynamics. Therefore, to test the accuracy of the model in predicting the behavior of isotropic solid particles in turbulence a set of experiments was conducted, where the effects of particle size and the density ratios will be tested.

A. Experimental setup

The aim of the experimental setup presented in Figure 1 was to generate near isotropic and homogeneous turbulence with no mean flow. In order to achieve this a pair of 1 × 1 m grids was built with 2 cm thick square bars into a mesh of size $H = 10$ cm. The two grids were placed at a distance $D_{ist} = 60$ cm apart in a water tank and were oscillated in phase at a frequency $f = 1.67$ Hz and a stroke $\Delta = 10$ cm.

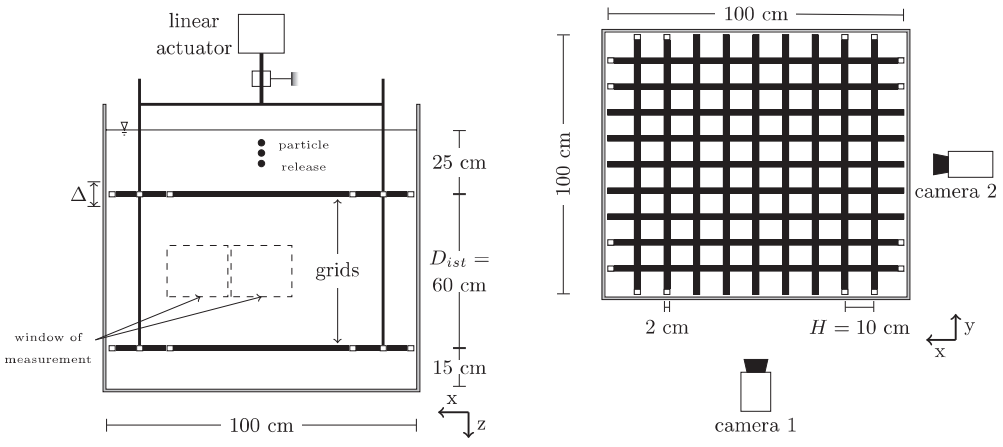

(a) Side view (b) Plan view

FIG. 1. Scheme of the double-grid setup (the origin of the axis is located on the bottom right corner in the center of the lower grid). PIV measurement are recorded with camera 1, and particle trajectories using both cameras 1 and 2.

B. Turbulent field properties

The turbulence generated by those grids was then quantified using particle image velocimetry (PIV) and two-dimensional laser doppler velocimetry (2D-LDV) measurements. These two techniques were chosen for the information on the turbulence they can provide. The PIV measurements were done for two 20 × 20 cm windows of measurement. One window was placed in the center of the tank, with its center at (50, 50, −30) cm, which is where the particles will be recorded and the other window with its center placed at (68, 50, −30) cm, which is closer to the edge of the tank. The second window allowed a comparison with the 2D-LDV results and to test the influence of the edge of the tank on the flow. A thousand pair of images were recorded with an interburst of 10 ms (i.e., the PIV measurements were recorded at frequency of 100 Hz). Each pair of recordings were done 1 s apart. Therefore the total time of the recordings is 1000 s, which is equivalent to almost 600 cycles of the oscillating grid. Furthermore, each recorded image had a spatial resolution of approximately 105 pixels/cm. The grid used by the PIV had a resolution of 8 pixels, which means the resolution used for the PIV measurement is equal 0.762 mm. Al-Homoud and Hondzo[22] suggest that ratio between the grid resolution of PIV (δ_{PIV}) measurements and the Kolmogorv length-scale (λ_s) should be smaller than 8. In this experiment, the Kolmogorv length-scale is approximately 0.4 mm, which means $\delta_{PIV}/\lambda_s = 2$. The 2D-LDV measurements were recorded at (65, 50, −30) cm with a frequency of 200 Hz for 1 h with a laser beam diameter of 2.2 mm.

The PIV measurements give instantaneous velocity fields, such as the one presented in Figure 2. From these velocity fields, the mean flow and the turbulent fluctuations can be calculated ($\overline{U_i}$ and U_i'). Yan *et al.*[23] and Al-Homoud and Hondzo[22] give methods to calculate the kinetic turbulent energy, k, and its dissipation rate, ε, which are needed to use the particle transport model presented in Sec. II D,

$$k = \frac{\overline{U_x'^2 + U_y'^2 + U_z'^2}}{2}, \tag{45}$$

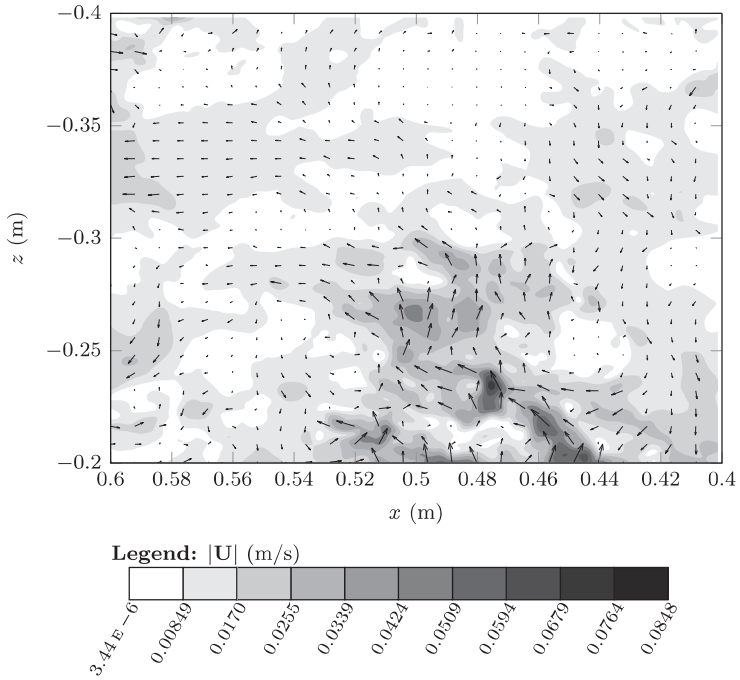

FIG. 2. An instantaneous velocity field recorded using PIV in two grids generated turbulence oscillating in phase at $f = 1.67$ Hz and $\Delta = 10$ cm.

$$\varepsilon = 3\nu \left[\overline{\left(\frac{\partial U_x'}{\partial x}\right)^2} + \overline{\left(\frac{\partial U_z'}{\partial x}\right)^2} + \overline{\left(\frac{\partial U_x'}{\partial z}\right)^2} + \overline{\left(\frac{\partial U_z'}{\partial z}\right)^2} + 2\overline{\left(\frac{\partial U_x'}{\partial z}\frac{\partial U_z'}{\partial x}\right)} + \frac{2}{3}\overline{\left(\frac{\partial U_x'}{\partial x}\frac{\partial U_z'}{\partial z}\right)} \right]. \tag{46}$$

Using the assumption that the flow is horizontally isotropic the value for U_y', used in Eq. (45), is taken to be equal to U_x'. The 2D-LDV measurements combined with the PIV measurements validated this assumption.

Using Eqs. (45) and (46), the turbulent properties required for particle transport can be plotted over the window of measurement, see Figure 4. The oscillating grid can cause the mean vertical fluid velocity to oscillate in phase with the grid oscillation frequency. This can create strong fluctuations, which become apparent when observing the energy spectrum calculated from the vertical fluid velocities LDV measurements, see Figure 3. As a reminder, the kinetic energy components of the flow can be calculated by applying the Fourier transform to the autocovariance of a fluid velocity component

$$E_{UU,i}(\omega) = \frac{1}{\pi}\int_{-\infty}^{\infty} R_{UU,i}(\tau) exp(-i\omega\tau)\, d\tau, \tag{47a}$$

$$R_{UU,i}(\tau) = \langle U_i(t)\, U_i(t+\tau)\rangle, \tag{47b}$$

where $E_{UU,i}$ is the kinetic energy as a function of the eddy angular frequency and $R_{UU,i}$ is the autocovariance of a fluid velocity component U_i.

There are debates in the scientific community on whether these strong vertical fluctuations should be considered turbulent. The authors have chosen to consider these effects as turbulent, and therefore when applying the model described in Sec. II, $\overline{U_z}$ is set to zero to remain consistent with this hypothesis. Furthermore, it was discovered that in this particular case that filtering out the grid oscillation frequency from the velocity measurements does not affect the results presented below.

The fields in Figure 4 are coarse, and for modeling purpose smooth empirical formulas have been developed as they can be extended outside of the window of measurement, to the point of

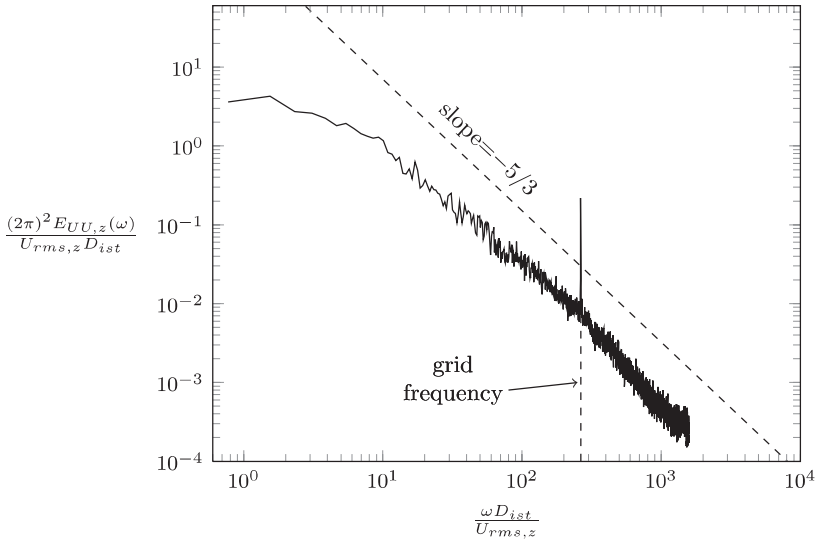

FIG. 3. The vertical energy spectrum obtained from 2D-LDV measurements of two oscillating grid generated turbulence with grid oscillating frequency $f = 1.67$ Hz and stroke $\Delta = 10$ cm. The energy ($E_{UU,z}$) is given as a function of the eddy angular frequency (ω).

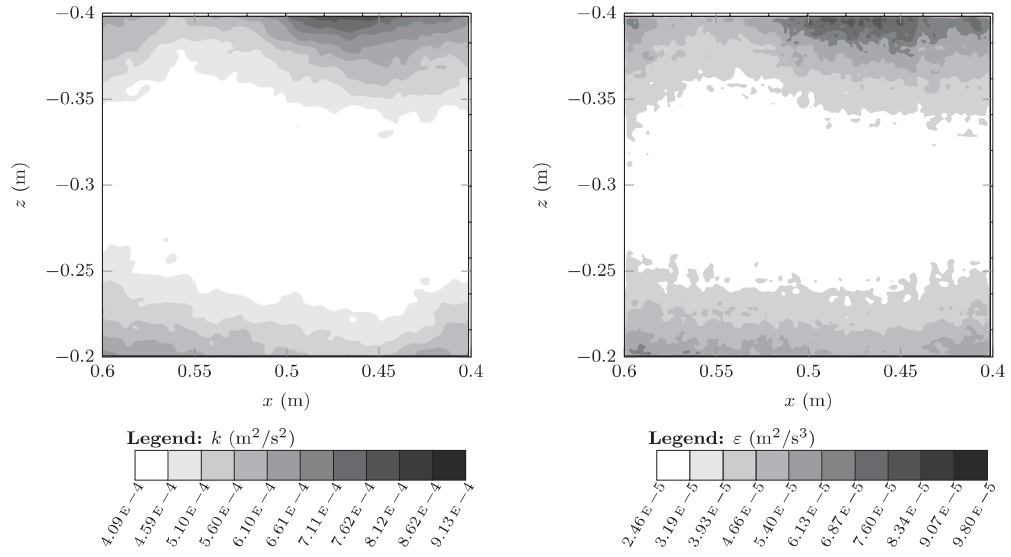

(a) Kinetic turbulent energy (k)

(b) Turbulent energy dissipation rate (ε)

FIG. 4. The mean kinetic energy and its mean dissipation rate for two oscillating grid generated turbulence with $f = 1.67$ Hz and $\Delta = 10$ cm.

release of the particles. In literature most studies of oscillating grids generated turbulence have been done for a single grid. These papers give empirical formulas for the spatial distribution of the root mean square of turbulent velocity fluctuations, as well as the kinetic turbulent energy and its dissipation rate.[22,24–26] Using the crude assumption that the turbulent kinetic energy of the two grids can be added, an empirical formula can be developed for two grid generated turbulence, where a free parameter will be adjusted to fit to the problem at hand

$$U_{rms,x} = \sqrt{\overline{U_x'^2}} = U_{rms,y} = \theta_1 H^{\frac{1}{2}} \Delta^{\frac{3}{2}} f \left[z^{-2} + (D_{ist} - z)^{-2} \right]^{\frac{1}{2}}, \tag{48a}$$

$$U_{rms,z} = \theta_2 H^{\frac{1}{2}} \Delta^{\frac{3}{2}} f \left[z^{-2} + (D_{ist} - z)^{-2} \right]^{\frac{1}{2}}, \tag{48b}$$

$$k = \frac{1}{2} \left(2\theta_1^2 + \theta_2^2 \right) H \Delta^3 f^2 \left[z^{-2} + (D_{ist} - z)^{-2} \right], \tag{48c}$$

$$\varepsilon = \frac{\theta_3 U_{rms,x}^3}{D_{ist}}. \tag{48d}$$

These equations have been developed by assuming that the turbulent eddies are dependent on the mesh size of the grid, the frequency and the amplitude of the oscillations and that they decrease away from the grid.

From the measurements of the case where the grids are oscillating in phase at a frequency $f = 1.67$ Hz and stroke $\Delta = 10$ cm the constants have been estimated to be $\theta_1 = 0.202$, $\theta_2 = 0.261$, and $\theta_3 = 5.60$. This therefore gives the profiles in Figure 5 for k and ε. One should note that the measured values of ε presented in this figure are probably underestimated along the edge of the window of measurement as its calculation requires the spatial derivatives of fluid velocity.

Two characteristic parameters of the turbulence are also given in Figure 5 as they can be used to provide relationships between the turbulent flow and the particles released. These parameters are the turbulent characteristic time T_L from Eq. (28a) and the characteristic size of the large turbulent eddies given by

$$\lambda_l = C_\mu^{3/4} k^{3/2} / \varepsilon. \tag{49}$$

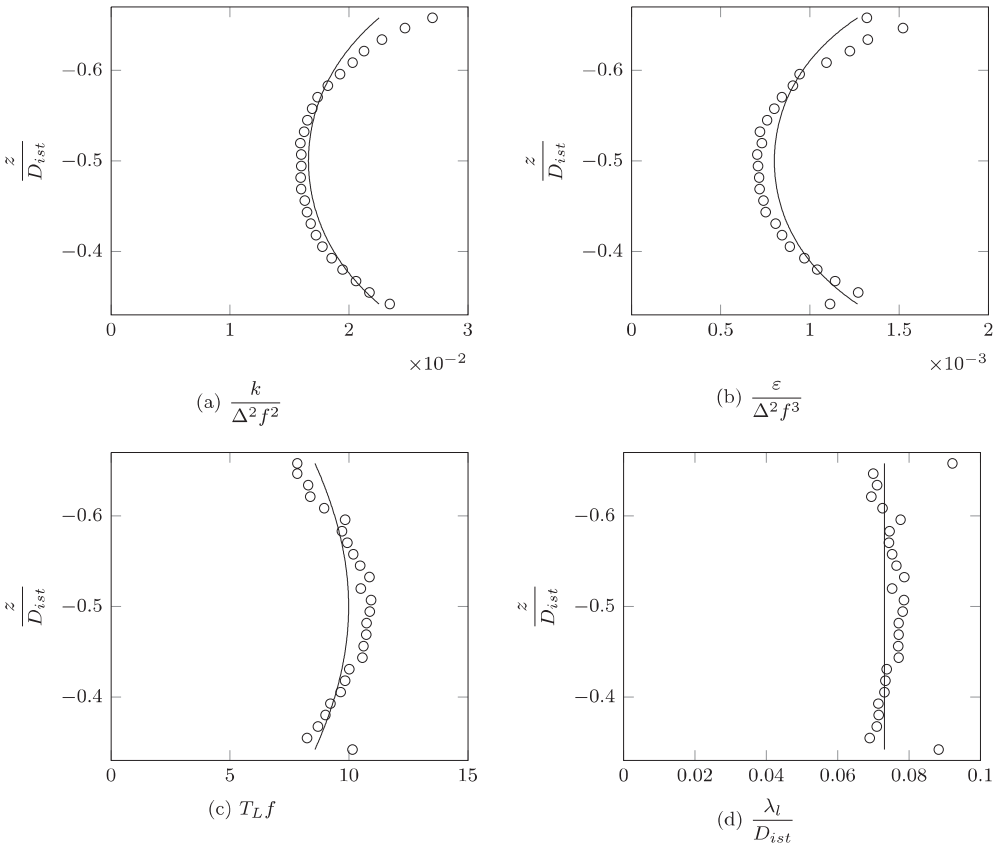

FIG. 5. Non-dimensional vertical profiles for the kinetic turbulent energy k, its dissipation rate ε, the turbulence characteristic time T_L, and the characteristic length of the large turbulent eddies λ_l. The circles represent horizontally averaged experimental results and the solid line represents the empirical profile found using Eqs. (48).

Equations (48), with the appropriate constants, allow therefore the mean turbulent flow properties to be reasonably estimated, which can then be inputted into the equations described in Sec. II D to predict particle transport. Furthermore, using the empirical values for k and ε from Eq. (48) the ratio λ_l/D_{ist} is equal to a constant and interestingly for highly turbulent flows $D/\lambda_l \sim \tau_{part}/T_L$.

From the results of k and ε, the mean Reynolds number of the turbulence inside the window of measurement can be calculated. As reminder it is in proportion to the ratio of the size of the large turbulent eddies over the size of the small turbulent eddies, and it can be calculated using the following equation:

$$R_t = \frac{k^2}{\varepsilon \nu}, \tag{50}$$

which for the current experiment is equal to about 6000.

The effect of the edges of the tank was also tested, to verify the presence of a mean flow. Table I summarizes the flow properties likely to be affected by the tank. From this table, we see that some boundary effects can be observed. The mean velocities would suggest that there are some recirculation close to the edge of the tank; however, as the particles are released in the center of the volume of measurement the mean flow velocity can be assumed to be equal to zero as they are an order under the velocity fluctuations. Furthermore, this table also shows that the turbulence is slightly more isotropic in the center of the tank than at the edge.

Further measurements were done using 2D-LDV, although for a different grid oscillation frequency. The oscillation used had a stroke of 6 cm and a frequency of 2.63 Hz. The results obtained

TABLE I. Summary of flow characteristics for a grid oscillation amplitude of 10 cm and a frequency of 1.67 Hz.

Position (cm)	$\overline{U_x}$ (m/s)	$\overline{U_z}$ (m/s)	$U_{rms,\,x}$ (m/s)	$U_{rms,\,z}$ (m/s)	$U_{rms,\,x}/U_{rms,\,z}$
(65, 50, −30)	−0.00220	−0.0125	0.0220	0.0302	0.729
(50, 50, −30)	−0.00158	−0.00423	0.0156	0.0196	0.795

TABLE II. Comparison between particle image velocimetry and two-dimensional laser doppler velocimetry measurements for a grid oscillation amplitude of 6 cm and a frequency of 2.63 Hz.

	$U_{rms,x}$ (m/s)	$U_{rms,z}$ (m/s)	k (m^2/s^2)
PIV	0.0113	0.0148	2.38×10^{-4}
2D-LDV	0.0103	0.0145	2.1×10^{-4}
$\frac{U_{rms,i,\mathrm{PIV}}}{U_{rms,i,\mathrm{2D\text{-}LDV}}}$	1.10	1.02	1.13
$\frac{U_{rms,i,\mathrm{PIV}}}{U_{rms,i,\mathrm{2D\text{-}LDV}}}$ in Al-Homoud and Hondzo[22]	1.20	1.40	1.58

from this setup can be compared to those with a stroke of 10 cm and a frequency of 1.67 Hz as the measured values are of the same order. This can be seen as the constants used in Eqs. (48) are $\theta_1 = 0.202$, $\theta_2 = 0.261$, and $\theta_3 = 5.60$ for $f = 1.67$ Hz and $\Delta = 10$ cm and $\theta_1 = 0.118$, $\theta_2 = 0.153$, and $\theta_3 = 11.7$ for $f = 2.63$ Hz and $\Delta = 6$ cm. The comparison with a punctual PIV value in Table II validates the values of the spatial PIV results. The same process was done in Al-Homoud and Hondzo,[22] and the difference ratios ($U_{rms,i,\mathrm{PIV}}/U_{rms,i,\mathrm{2D\text{-}LDV}}$) are also shown in Table II. Furthermore, Al-Homoud and Hondzo[22] calculated the anisotropy ratio ($U_{rms,x}/U_{rms,y}$) to be 1.05, whereas in this experiment it is 0.75.

C. Particle tracking

Different spheres of Nylon Polyamide PA 6,6 (see Table III) were released 20 cm above the oscillating grids (see Figure 1(a)). Two different fluids, of densities $\rho_f = 1000$ and 1084 kg/m^3, were used. For each run 25 particles will be released in the experimental setup.

An updated Stokes number will also be introduced. Unlike the number presented in Eq. (2a), which only compared the relaxation time of particles experiencing Stokes drag to the small turbulent eddies, this number will show the impact of the turbulent eddies for settling particles using the characteristic times introduced in Eqs. (27a) and (27b),

$$\mathrm{St}_{set} = \frac{\tau_{part}(\mathbf{V} = -V_{set}\mathbf{e_z})}{T_L}. \tag{51}$$

This Stokes number introduces the concept of the settling velocity V_{set}, for which the relaxation time of a particle is calculated. This velocity is the maximum velocity a body falling unhindered through the fluid can reach. It can be calculated using Eq. (13) by considering that a particle has reached its settling velocity when it has stopped accelerating, and therefore it is given by the

TABLE III. The diameters and densities of the Nylon Polyamide PA 6,6 particles.

Diameter D (mm)	Standard deviation of D (%)	Mean density ρ_s (kg/m^3)	Standard deviation of ρ_s(%)	Stokes number St_{set}	Volume fraction of particles Ω_f
20	0.254	1129	0.0740	2.37	1.05×10^{-4}
10	0.508	1128	0.301	0.868	1.31×10^{-5}
5	1.02	1115	0.125	0.677	1.63×10^{-6}
2	2.54	1062	2.42	0.616	1.05×10^{-7}

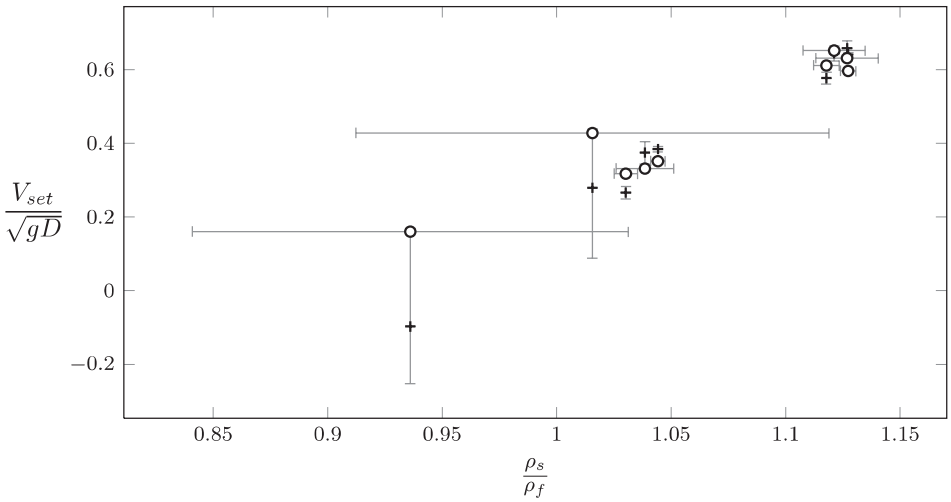

FIG. 6. Dimensionless settling velocities for the particles described in Table III and for fluid densities $\rho_f = 1000$ and 1084 kg/m^3. The plus symbols show the analytical solution (Eq. (52)) and the circles show the experimental measurements. The horizontal gray bars are the 95% confidence interval error bars for the experimental density ratios and the vertical gray bars are the 95% confidence interval error bars for the analytical velocities using these ratios.

following implicit formula:

$$V_{set} = \frac{|m - \rho_f \Omega|}{(m - \rho_f \Omega)} \sqrt{\frac{2\,|m - \rho_f \Omega|}{\rho_f S C_D(\mathrm{Re}_{set})} g_z}, \tag{52}$$

where $\mathrm{Re}_{set} = |V_{set}|\, D/\nu$.

In Table III, the Stokes number is calculated using the settling velocities for each particle in a water of density 1000 kg/m^3 and the mean turbulence characteristic time of Figure 5. Since all these values are of the same order as 1 the turbulence effects and the particle properties need to be considered for all particle size. In addition, since the Stokes number is greater for the larger particles, the properties of the bodies will have a greater effect. The settling velocities for all these particles, released in waters of densities $\rho_f = 1000$ and 1085 kg/m^3, are plotted in Figure 6. Furthermore, the values for the volume fraction number presented in this table indicate that the larger particles might affect the turbulence slightly, and that the one way fluid-particle coupling might not be accurate anymore.

The trajectories for the particles released into the flow described in Sec. III A were measured using two cameras placed perpendicularly to each other. The volume of measurement, located in the center of the two grids, had a shape close to a cube $20 \times 20 \times 20$ cm^3, but of a shape similar to the one presented in Figure 7.

The shape of the volume of measurement described in Figure 7 shows that a linear relationship needs to be assumed to convert particle position from pixel to millimeter,[27] see Eqs. (53):

$$\text{Camera 1:} \quad \frac{X_x(mm)}{X_x(pixels)} = \alpha_y X_y(mm) + \beta_x \;; \quad \frac{X_{z_1}(mm)}{X_{z_1}(pixels)} = \alpha_y X_y(mm) + \beta_x, \tag{53a}$$

$$\text{Camera 2:} \quad \frac{X_y(mm)}{X_y(pixels)} = \alpha_x X_x(mm) + \beta_y \;; \; \frac{X_{z_2}(mm)}{X_{z_2}(pixels)} = \alpha_x X_x(mm) + \beta_y. \tag{53b}$$

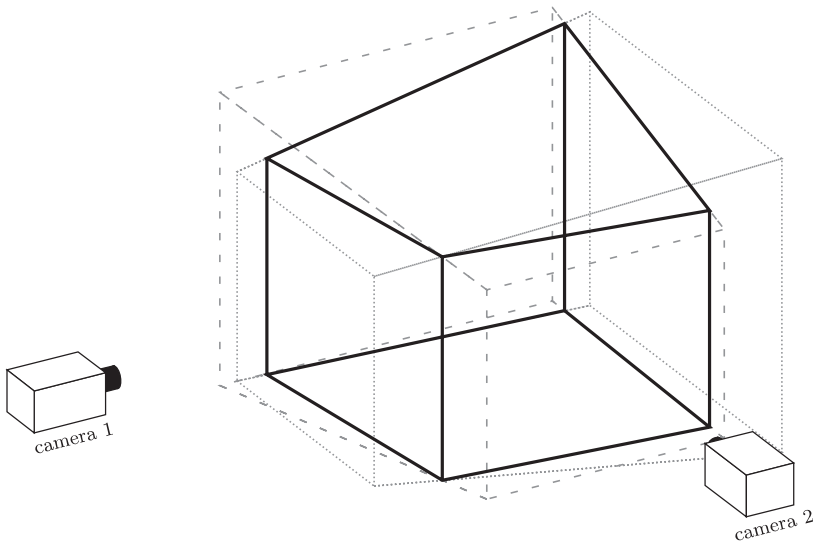

FIG. 7. Volume of measurements for the two perpendicular cameras recording falling bodies. The densely dotted gray lines show the volume recorded by camera 1, the loosely dashed gray lines show the volume recorded by camera 2 and the thick solid black lines show the volume of measurement common in the two cameras.

Obviously in Eqs. (53), the particle position X_z should be equal in cameras 1 and 2 ($X_{z_1} = X_{z_2}$). The coefficients α_i and β_i need to be calibrated by recording known positions of an object inside the volume of measurement.

Furthermore, the shape and size of the volume recorded by a camera implies that particles seen by one camera might not be seen by the other, see Figure 8 which shows an example of associated particles.

IV. MODEL VALIDATION

From these records of particle trajectories, it is possible to obtain an estimate of the particle velocities looking at the displacement in between two recorded images. These particle velocities can be compared to the results obtained using the stochastic numerical model developed in Sec. II D, in combination with the empirical model of Sec. III B used as the mean flow properties,

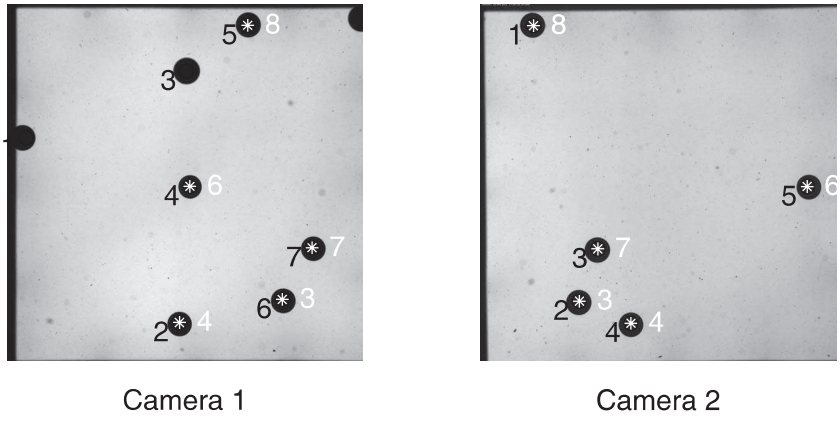

FIG. 8. Example of particles recorded for the two cameras. The number in black is a recognized particle in an image and the number in white, next to a white star, is a particle present in both cameras.

TABLE IV. Summary of the different models compared and different forcing considered.

	Model I	Model II	Model III	Model IV	Brownian motion
Crossing trajectories	Yes	No	No	No	No
Basset	Yes	Yes	No	No	No
Momentum	Yes	Yes	Yes	No	No
Drag	Yes	Yes	Yes	Yes	No
Source	Eq. (26)	Eq. (13)	see Ref. 11	see Ref. 5	Eq. (54)

and comparing the velocity statistics of numerical particles present in a volume of measurement similar to the experiment.

The results will be compared using the complete model presented in Sec. II D, for which the crossing trajectories effect can be found using the empirical values of $U_{rms,i} = \sqrt{\overline{U_i'^2}}$ and the settling velocity as the mean velocity difference between the fluid and the particle $V_{set} = \left|\overline{\mathbf{V}} - \overline{\mathbf{U}}\right|$, and therefore the main drift is in the z direction. It will then be tested against several models where the fluid velocity observed by the particle is assumed to be equal to the fluid velocity $\mathbf{U}^* = \mathbf{U}$. In these models, different levels of description of the solid body dynamics will be assessed. There will be the full description of the solid body dynamics presented in Sec. II B, a model similar to the one presented in this paper, but where the Basset history force is not accounted for Ref. 11, another model designed for small particles where the inertial properties of the body are reduced to the drag force[5] and a model where all the physical properties of the body are ignored and turbulence is modeled in a coarser fashion (Brownian motion[12]). As a reminder, in Brownian motion the transport equation is given by the following equation:

$$dX_i = \left[\overline{U_i} + \frac{C_\mu}{\sigma_c}\frac{\partial}{\partial x_i}\left(\frac{k^2}{\varepsilon}\right)\right]dt + \sqrt{2\frac{C_\mu}{\sigma_c}\frac{k^2}{\varepsilon}}dW_i, \tag{54}$$

where $C_\mu = 0.09$ and $\sigma_c = 0.72$, as was defined in Issa *et al.*[12]

A summary of the different models analysed is given in Table IV.

Figure 9 shows representative pdf of the horizontal and vertical velocities. Each plot of this figure is associated with five characteristic numbers: D/λ_l which shows the ratio of the particle diameter D to the characteristic length of the large turbulent eddies λ_l given by Eq. (49), ρ_s/ρ_f which gives the density ratios, the Stokes number St_{set} given by Eq. (51), N_r which is the number of experimental velocity records and Re_{set} which is the particle Reynolds number for particles at settling velocity. The pdf of the velocities are calculated using the velocity at every time step that a particle is present in the volume of measurement. N_r is then found using every recorded velocity along every trajectories of the particles. Only half of the horizontal velocity statistics are shown, as they are symmetrical around the mean velocity (0 m/s as there is no flow).

From Figure 9, it is possible to conclude that the vertical displacement is driven by the buoyancy effects, as it is of the same order as the settling velocity, whereas the horizontal velocities are smaller than the settling velocities, and therefore are driven by the turbulence. Second, this figure shows that the simplification of the transport of isotropic particles in turbulence to Brownian motion,[12] as is done commonly for contaminant transport,[28–30] cannot model accurately the turbulent diffusion of these particles, and it overestimates greatly the diffusion (the dotted lines in Figure 9 are very flat curves). Furthermore, the two particle transport models which ignore the Basset History force (the models III and IV in Table IV), give very similar results, which would indicate that momentum and added mass of the body can be neglected, especially for small bodies. For both of these models the horizontal displacement statistics are fairly well modeled, but the vertical (settling) statistics are not modeled as accurately. However, when the Basset History force (model II in Table IV)

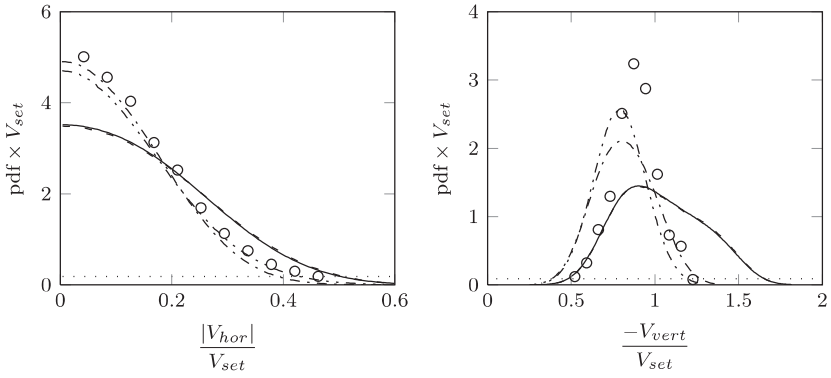

(a) $\frac{D}{\lambda_l} = 0.106$, $\frac{\rho_s}{\rho_f} = 1.12$, $\mathrm{St}_{set} = 1.52$, $N_r = 354$, $\mathrm{Re}_{set} = 620$

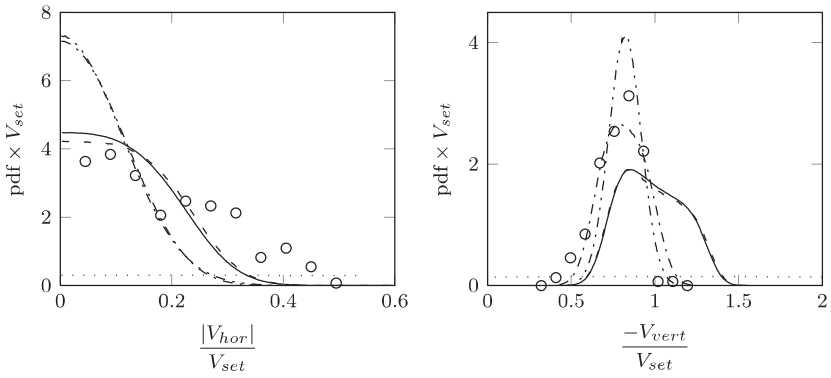

(b) $\frac{D}{\lambda_l} = 0.212$, $\frac{\rho_s}{\rho_f} = 1.13$, $\mathrm{St}_{set} = 2.06$, $N_r = 178$, $\mathrm{Re}_{set} = 2020$

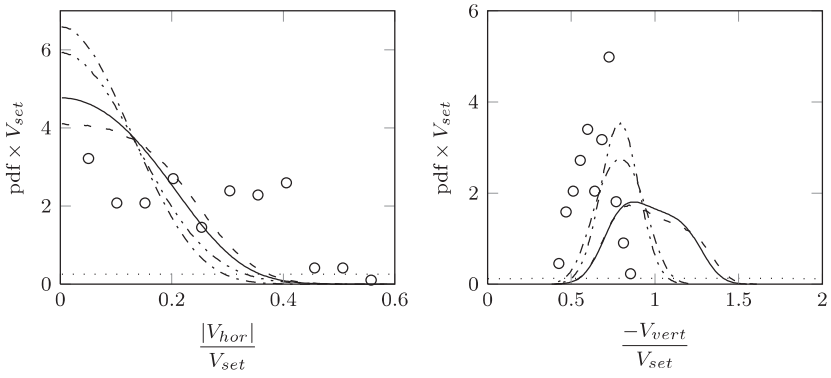

(c) $\frac{D}{\lambda_l} = 0.424$, $\frac{\rho_s}{\rho_f} = 1.047$, $\mathrm{St}_{set} = 4.58$, $N_r = 105$, $\mathrm{Re}_{set} = 3450$

FIG. 9. Probability density functions for particle velocities present inside the volume of measurement. The circles show the pdf of the experimental results, the dashed-dotted-dotted lines show the pdf for model I, the dashed-dotted lines show the pdf for model II, the solid lines show the pdf for model III, the dashed lines show the pdf for model IV, and the dotted lines show the pdf for Brownian motion. See Table IV for details on the models.

is included the model shows very good correlation to the experimental results for small particles, but as particles become bigger the model loses accuracy. This is expected as the formulation of the Basset History force chosen is designed for small particles, and the bigger particles were modeled to test the limitations of the model. Nonetheless considering the Basset History force

gives better probability density functions in the vertical direction, which is the main direction of motion.

In addition, the "crossing trajectories effects" mentioned by Csanady[8] and accounted for in model I using Eq. (21) (see Table IV) reduces the spread of velocity probability density functions shown in Figure 9. This is expected because the crossing trajectories effects increases the decorrelation between the fluid and the solid particle, and this way a solid body does not follow completely the turbulent eddies. Nonetheless, the effect of these crossing trajectories has only a little effect on the standard deviation of the horizontal velocity pdf shown in Figure 9. From this result, in two-dimensional horizontal simulations, the decorrelation between a solid body and a fluid particle due to gravity effects can be ignored. However, it has been proven that the "crossing trajectories effects" might not always be negligible and more research will need to be conducted to consider the decorrelation occurring from inertial effects. Still, focusing on an accurate modelisation of the solid body dynamics gives a reasonable estimates of the motion of solid particles as there are no great differences between the pdf of models I and II (only the height of the peak in the vertical velocity pdf, but not the location).

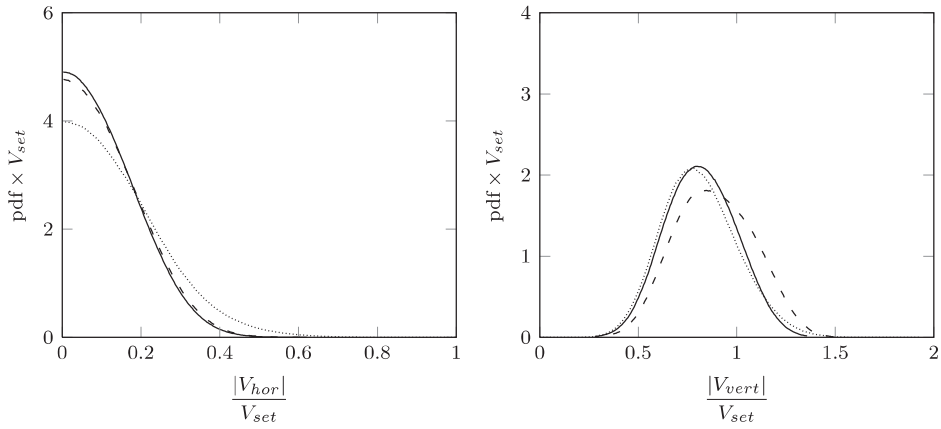

(a) $\frac{D}{\lambda_l} = 0.106,\ \frac{\rho_s}{\rho_f} = 1.12,\ St_{set} = 1.52$

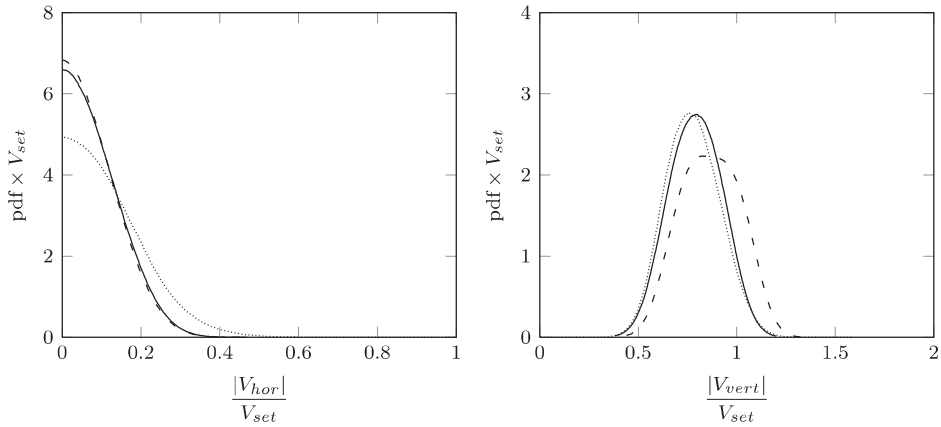

(b) $\frac{D}{\lambda_l} = 0.424,\ \frac{\rho_s}{\rho_f} = 1.047,\ St_{set} = 4.58$

FIG. 10. Probability density functions for numerical particle velocities present inside the volume of measurement transported using the model described in Eq. (52). The solid lines show the pdf for particles with $\mathbf{V_0} = 0$, the loosely dashed lines show the pdf for particles with $V_{0,z} = \frac{1}{2}V_{set}$ and the densely dotted lines show the pdf for particles with $\langle \mathbf{V_0} \rangle = 0$ and $\langle \mathbf{V_0}^2 \rangle = Sf$.

All of the numerical vertical statistics have a bigger spread and mean than the experimental results, and this effect becomes more apparent for the larger particles (plotted in Figure 9(c)). One of the reasons for these differences is probably because as particles are bigger than the initial hypotheses developed in Sec. II B, specifically that the bodies do not affect the flow, become inappropriate and the experimental results do not correspond as well to the experimental data.

An other source of differences between experimental and numerical values could also originate from the relaxation time of the bodies. The relaxation time represents the time a particle will forget the boundary conditions. A quick calculation of the relaxation time once settling velocity is reached (Eq. (52)) and the time a particle would take to settle (without any turbulence) from rest to the top of the volume of measurement t_{set}, would give for the parameters of Figure 9(a) $\tau_{part}/t_{set} = 4.12$, for those in Figure 9(b), $\tau_{part}/t_{set} = 5.56$ and for those in Figure 9(c), $\tau_{part}/t_{set} = 7.70$. These values are likely to be smaller in the case of the experiment as the particles enter the fluid with an initial velocity, and their fall is slowed down by the turbulence. Nonetheless, from these ratios, it is possible to conclude that the biggest particles ($D/\lambda_l = 0.424$) are likely to have kept in memory the effect of the oscillating grids as they pass through. This could mean that the experimental result in Figure 9(c) might just show a transport of the initial boundary conditions. This is reinforced by the fact that the mean vertical velocities for the experimental results shown in Figures 9(b) and 9(c) are lower than the settling velocity described in Eq. (52); therefore, particles have not finished accelerating and have kept in memory the initial boundary conditions (i.e., passing through the top oscillating grid or accelerating from rest).

To verify this hypothesis numerical tests were done with the inertial model developed in this paper. Particles were released at a known height, 10 cm below the center of the top oscillating grid. Different initial particle velocities, $\mathbf{V_0}$ were tested: particles starting at rest, particles with an imposed initial vertical velocity equal to half the settling velocity and particles where the initial velocities are generated through a random distribution with mean equal to zero and a standard deviation equal to half the stroke times the frequency of grid oscillations, to simulate impact of the grids on the particles. Statistics are plotted in Figure 10.

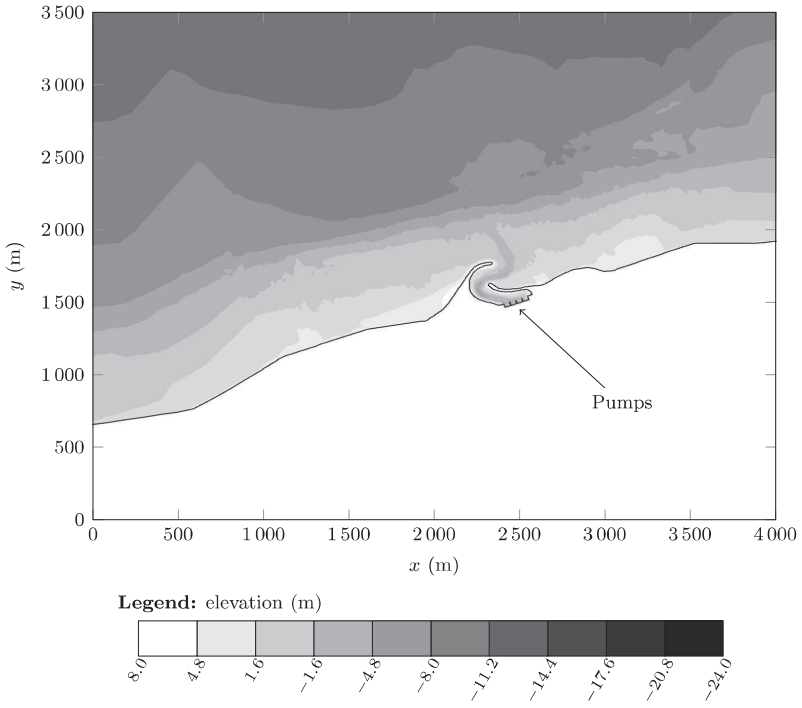

FIG. 11. A complex bathymetry used to model the flow around an industrial structure pumping sea water.

Figure 10 shows that imposing an initial velocity distribution or an initial vertical settling velocity will modify the distribution of the velocities for both size of particles. This is more visible for the large particles, but it is still visible for small particles. This is probably because in the numerical simulations presented in this figure particles were released very close to the volume of measurement, as the empirical model for the mean flow characteristics (Eqs. (48)) cannot be applied much further above the volume of measurement.

Finally, the finite size of the body has a filtering effect on the turbulence, as the turbulent eddies of size smaller than the particle will not affect the dispersion. This filtering effect is further emphasized by the inertial properties of the body as the particle relaxation time will limit the impact of the turbulent eddies, which is in accordance to what Yeo *et al.*[10] have observed.

V. APPLICATION TO ENVIRONMENTAL STUDIES

The difference between each model presented in Figure 9 needs to be understood in order to provide accurate models in environmental flow. The case presented in Figure 11 of a schematic harbor with a realistic bathymetry pumping sea water will be used as an example.

A large scale model is necessary to provide a flow regime for environmental problems, such as the one illustrated in Figure 11 where the effects of the pumps, tides, or waves are significant. However, the solid bodies of interest in these flows usually tend to be much smaller than the mesh size of the model for this kind of flow. This is why often in this kind of model, a Lagrangian stochastic model is usually applied; however, most existent environmental models tend to neglect some body properties. For example, Issa *et al.*[12] and Monti and Leuzzi[30] model particle transport using Brownian motion and Salomonsen *et al.*[6] assumes that particles follow exactly the fluid. Other

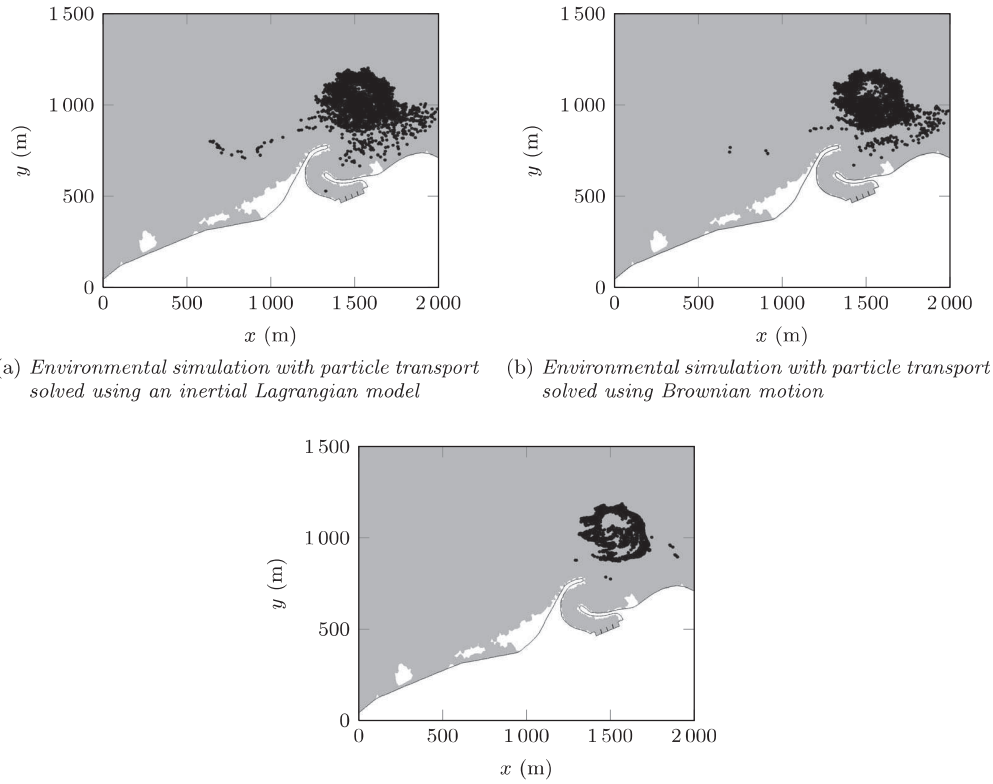

(a) *Environmental simulation with particle transport solved using an inertial Lagrangian model*

(b) *Environmental simulation with particle transport solved using Brownian motion*

(c) *Environmental simulation with particle transport following exactly mean fluid velocity*

FIG. 12. Illustration of the importance of including the body properties in environmental simulations.

better models exist, such as the inertia free model in Peirano *et al.*[21] or van Aartrijk,[31] but these focus on small particles and are not applied to large environmental simulations.

Figure 12 illustrates the differences in particle transport models for the bathymetry of Figure 11 where the flow regime is solved using a finite element shallow water equation solver, with depth-integrated k-ε closure. It shows that including the properties of the bodies (drag, inertia) will increase greatly the diffusion of these bodies, and therefore the possibility for these bodies to enter the harbor channel.

It should be restated that the results shown in Figure 12 are completely qualitative and, therefore, are not validated. However, if the inertial properties of the particles of interest could be neglected the Lagrangian transport model presented in this paper should fall back onto Brownian motion. The fact that there exists a difference gives voice to the fact that research into consideration of inertial properties for bodies in environmental flows is necessary.

VI. CONCLUSION AND FUTURE WORK

A solid particle transport model has been developed here to be used in cases of low concentrations of solid bodies transported in a fluid over a large area. This model has the advantages of considering key physical properties of the bodies for this kind of problem as well as having a more developed approach to model turbulence than simple Brownian motion. This model can easily be attached to an industrial flow modeler as it is independent of the numerical time step.[11]

A simple test case was performed to test the accuracy of the model for isotropic solid particles in semi-isotropic turbulence. The experimental results show that for particles corresponding to the hypotheses set by the model, the numerical results seem to be in accordance to the experimental values. Furthermore, it seems that the two key physical properties of the particles are the Basset History and the drag forces. The "crossing trajectories effects" resulting from the effect of gravity were also taken into account. These expectedly reduced the diffusive effects of the turbulence, but did not have a significant impact horizontal spread. Furthermore, they did not modify radically the probability density functions, and it can be assumed that they have a minor effect on the motion of a solid particle. Therefore, until further research has been done into the crossing trajectories effect from inertial properties of the bodies, it is assumed that these effects can be ignored for two-dimensional horizontal simulations. Moreover, ignoring the crossing trajectory effects allows a simpler model to be used to predict the mean flow properties, which is more in accordance to the tools available to model large environmental coastal flows.

In addition, the experimental results indicate that the transport model for this class of particle is more dependent on the physical properties of the particle than on the turbulent diffusion model differentiating from other work on solid particle transport, such as the work done by Csanady,[8] Minier and Peirano,[5] Sawford and Guest,[9] or Yeo *et al.*[10]

These result then lead to several tests that need to be done in the future. First, a flow regime in better accordance to real problematics need to be tested. This will allow to test a hybrid stochastic transport model, where the flow regime is modeled using an industrial code and the particle transport is tested using the model developed in this paper, and further validated this model in a more complex problem than semi-isotropic quasi-homogeneous turbulence. This model was developed to be applicable to problems close to algae transport in coastal waters, which are non-isotropic and strongly inhomogeneous.

ACKNOWLEDGMENTS

The authors would like to thank Dr. Jean-Pierre Minier for his help developing the numerical model.

[1] S. Elghobashi, "An updated classification map of particle-laden turbulent flows," in *Proceedings of the IUTAM Symposium on Computational Multiphase Flow*, edited by S. Balachandar and A. Prosperetti (Springer, 2006).
[2] J. K. Eaton and J. R. Fessler, "Preferential concentration of particles by turbulence," Int. J. Multiphase Flow **20**, 169–209 (1994).

[3] C. Poelma, J. Westerweel, and G. Ooms, "Particle-fluid interactions in grid-generated turbulence," J. Fluid Mech. **589**, 315–351 (2007).
[4] M. Uhlmann, "Interface-resolved direct numerical simulation of vertical particulate channel flow in the turbulent regime," Phys. Fluids **20**, 053305 (2008).
[5] J.-P. Minier and E. Peirano, "The pdf approach to turbulent polydispersed two-phase flows," Phys. Rep. **352**, 1–214 (2001).
[6] J. Salomonsen, M. Flindt, O. Geertz-Hansen, and C. Johansen, "Modelling advective transport of Ulva lactuca (L) in the sheltered bay, Møllekrogen, Roskilde Fjord, Denmark," Hydrobiologia **397**, 241–252 (1999).
[7] P. Donaghay and T. Osborn, "Toward a theory of biological-physical control of harmful algal bloom dynamics and impacts," Am. Soc. Limnol. Oceanogr. **42**, 1283–1296 (1997).
[8] G. T. Csanady, "Turbulent diffusion of heavy particles in the atmosphere," J. Atmos. Sci. **20**, 201–208 (1963).
[9] B. L. Sawford and F. M. Guest, "Lagrangian statistical simulation of the turbulent motion of heavy particles," Boundary-Layer Meteorol. **54**, 147–166 (1991).
[10] K. Yeo, S. Dong, E. Climent, and M. R. Maxey, "Modulation of homogeneous turbulence seeded with finite size bubbles or particles," Int. J. Multiphase Flow **36**, 221–233 (2010).
[11] A. Joly, "Modelling of the transport of algae in a coastal environment using a stochastic method," Ph.D. dissertation (Université Paris-Est, 2011).
[12] R. Issa, D. Roug, M. Benoit, D. Violeau, and A. Joly, "Modelling algae transport in coastal area with the shallow water equations," J. Hydro-Environment Res. **3**, 215–223 (2009).
[13] S. Pope, *Turbulent Flows* (Cambridge University Press, Cambridge, 2000).
[14] C. Gardiner, *Handbook of Stochastic Methods* (Springer-Verlag, Berlin, 2004).
[15] S. B. Pope, "Lagrangian PDF methods for turbulent flows," Annu. Rev. Fluid Mech. **26**, 23–63 (2004).
[16] T. R. Auton, J. C. R. Hunt, and M. Prud'homme, "The force exerted on a body in inviscid unsteady non-uniform rotational flow," J. Fluid Mech. **197**, 241–257 (1988).
[17] M. R. Maxey and J. J. Riley, "Equation of motion for a small rigid sphere in a nonuniform flow," Phys. Fluids **26**, 883–889 (1983).
[18] P. Bagchi and S. Balachandar, "Effect of free rotation on the motion of a solid sphere in linear shear flow at moderate Re," Phys. Fluids **14**, 2719–2737 (2002).
[19] M. A. T. van Hinsberg, J. H. M. ten Thije Boonkkamp, and H. J. H. Clercx, "An efficient, second order method for the approximation of the Basset history force," J. Comput. Phys. **230**, 1465–1478 (2011).
[20] J. Almedeij, "Drag coefficient of flow around a sphere: Matching asymptotically the wide trend," Powder Technol. **186**, 218–223 (2008).
[21] E. Peirano, S. Chibbaro, J. Pozorski, and J.-P. Minier, "Mean-field/PDF numerical approach for polydispersed turbulent two-phase flows," Prog. Energy Combust. Sci. **32**, 315–371 (2006).
[22] A. Al-Homoud and M. Hondzo, "Energy dissipation estimates in oscillating grid setup: LDV and PIV measurements," Environ. Fluid Mech. **7**, 143–158 (2007).
[23] J. Yan, N.-S. Cheng, H.-W. Tang, and S. K. Tan, "Oscillating-grid turbulence and its applications: a review," J. Hydraul. Res. **45**, 26–32 (2007).
[24] I. P. D. De Silva and H. J. S. Fernando, "Oscillating grids as a source of nearly isotropic turbulence," Phys. Fluids **6**, 2455–2464 (1994).
[25] N.-S. Cheng and A. W.-K. Law, "Measurements of turbulence generated by oscillating grid," J. Hydraul. Eng. **127**, 201–208 (2001).
[26] M. Holzner, A. Liberzon, M. Guala, A. Tsinober, and W. Kinzelbach, "Generalized detection of a turbulent front generated by an oscillating grid," Exp. Fluids **41**, 711–719 (2006).
[27] P. Cordeiro Fernandes, "Étude expérimentale de la dynamique de corps mobiles en ascension dans un fluide peu visqueux," Ph.D. dissertation (INP Toulouse, 2005).
[28] A. Heemink, "Stochastic modelling of dispersion in shallow water," Stochastic Hydrol. Hydraul. **4**, 161–174 (1990).
[29] J. W. Stijnen, A. Heemink, and H. X. Lin, "An efficient 3D particle transport model for use in stratified flow," Int. J. Numer. Methods Fluids **51**, 331–350 (2006).
[30] P. Monti and G. Leuzzi, "Lagrangian models of dispersion in marine environment," Environ. Fluid Mech. **10**, 637–656 (2010).
[31] M. van Aartrijk, "Dispersion of inertial particles in stratified turbulence," Ph.D. dissertation (TU Eindhoven, 2008).